crystals

MDPI

Article

Mechanical and Microstructural Behavior of Tempered CPM® 3V High-Density Sintered Tool Steel

Stephen A. C. Hanson * and Sudhakar Vadiraja

Department of Materials Science and Engineering, Montana Technological University, Butte, MT 59701, USA
* Correspondence: shanson@mtech.edu

Abstract: The tempering response of CPM® 3V tool steel was investigated via a hardening and tempering heat treatment, tensile testing, fractography, and microstructural evaluation. CPM® 3V tool steel is manufactured using Crucible Particle Metallurgy (CPM®), a proprietary high-density sintering technique developed by Crucible Industries. The hardening and tempering heat treatments were applied to ASTM E8 standard test specimens. Tempering temperature was the experimental variable. The following samples were prepared: As-Hardened (no tempering); tempered at 450 °C, 550 °C, 650 °C, and 700 °C; and As-Received (annealed). Ultimate tensile strength and the yield strength of each treatment was determined using the ASTM E8 standard tensile test. The failed specimens were examined for mode of fracture at macro- and microscopic scales. Reflected light microscopy and a scanning electron microscope (SEM) was used for microstructural characterization. Testing and analysis established the samples tempered at <550 °C were dominated by brittle failure while samples tempered at >550 °C experienced ductile failure. The 550 °C treatment showed mixed ductile and brittle fracture features. This study found that CPM® 3V can be optimized for strength, with good tensile toughness, at a 550 °C tempering temperature. This is consistent with Crucible Industries' recommended tempering temperature for good wear resistance and toughness.

Keywords: tool steel; tempering response; tensile testing; steel microstructures; carbides; fractography; mechanical testing

Citation: Hanson, S.A.C.; Vadiraja, S. Mechanical and Microstructural Behavior of Tempered CPM® 3V High-Density Sintered Tool Steel. *Crystals* **2022**, *12*, 1670. https://doi.org/10.3390/cryst12111670

Academic Editors: Peng Chen, Feng Shi and Xiao-Wu Li

Received: 20 October 2022
Accepted: 16 November 2022
Published: 19 November 2022

1. Introduction

1.1. CPM® 3V and Tool Steels

Crucible Industries, a manufacturer of powder steels, produces CPM® 3V using their proprietary Crucible Powder Metallurgy (CPM®) technology [1]. CPM® technology uses high-density sintering of pre-alloyed particles to produce a material with uniform fine primary carbide distribution in a fine-grained iron (Fe) matrix [1]. Due to the proprietary nature of manufacturing CPM® steels, there is no additional information available regarding Crucible Industries' process.

CPM® steels have an exceptional combination of properties that are a result of well-dispersed, fine carbides in the microstructure that do not act as stress risers. This microstructure is achieved by the sintering process and is not attainable with conventional foundry techniques for high-alloy steels. For example, it is generally recommended that cast or continuously cast alloy grades do not contain more than 2 weight percent (wt.%) vanadium (V) [2]. However, the CPM® process that Crucible Industries uses can produce alloys that have V content exceeding 13 wt.%. CPM® 3V steel nominally contains 2.75 wt.% V; the CPM® 3V specimens tested in this study measured 2.53 wt.% V (Table 1). Increasing the alloy composition is possible in sintered powder metallurgy steels because the process of sintering the powder is a solid-state, diffusion-based process. The mechanisms of atomic mobility are notably different for solid and liquid states of matter, leading to much lower rates of diffusion in solid-state processes [3]. With decreased diffusion rates, the abundance of alloy elements that have strong carbide affinity can be increased without the formation of

large carbides, sheet like carbides, or other carbide morphologies which are usually found in foundry-cast, high-alloy steel [2,4]. Sintering is also conducted under pressure. This increased pressure serves to increase the particle adhesion, increase pseudo-viscous flow of the porous powder bed, and increase the effective density within the sintering powder bed [3,5]. Hot isostatic pressing or hot-working post-sintering treatments can be done to reduce the porosity of the sintered materials [6]. CPM® 3V steel is a high-density (low porosity) sintered steel.

Table 1. Composition of CPM® 3V tool steel from Arc/Spark-OES bulk composition analysis (all numerical values given in wt.%).

Steel Alloy	C	Si	Mn	Cr	Mo	V	P	S	Balance of Fe
CPM® 3V	0.71	0.84	0.38	7.81	1.32	2.53	0.0115	0.0138	86.38

Tool steels, in general, have a variety of applications in industry and manufacturing. Many tool steels have significant alloy proportion for improved mechanical properties and high-temperature performance. Due to the increased cost of alloying elements, tool steels are used in critical applications. CPM® 3V is a tool steel that is designed and produced for high toughness and high wear-resistance applications [1]. The high toughness and high wear-resistance properties enable CPM® 3V steel to be a good option for stamping/forming tools, punches and dies, blanking tools, industrial knives, shear blades, scrap choppers, industrial pelleting blades, plastic injection molding feed screws, dies, and valve components in systems that carry abrasive slurries [1].

Typically, toughness and wear-resistance are inversely related. For example, S7 tool steel has high toughness and low wear-resistance. CPM® 3V has comparable wear resistance to D2 and CRU-WEAR steels while having much greater toughness [1]. However, without the proper heat treatment, optimal performance of the material cannot be obtained. Establishing the tempering response of specific alloys is important to achieving maximum life and performance out of components. In many tool steel applications, failures occur prematurely due to chipping [7,8]. Therefore, a tool steel that has a combination of high toughness and high wear resistance is desirable.

1.2. Hardening and Tempering Steels

Hardening steel is the first step to improving the performance of the steel in high strength applications. The most basic iron-carbon (Fe-C) system is hardenable at 0.025–2.0 wt.% carbon (C). Steel and tool steel typically have $\leq$~2 wt.% C because the high temperature Fe-phase, austenite, can only dissolve $\leq$~2 wt.% C. In contrast, the low temperature Fe-phase, α-ferrite, contains a maximum of ~0.025 wt.% C [8]. The difference in maximum C wt.% in the two Fe-phases plays a key role in the hardenability of steel.

Austenitization is when the material is heated to a temperature where the stable phase is austenite and is held there for a period of time (soaking). Soaking ensures that the material is uniformly heated, forming face-centered-cubic (FCC) austenite and allowing all alloying elements to completely or partially dissolve in the austenite phase. Cooling slowly from the austenite phase field allows the material to maintain equilibrium conditions so that the excess carbon and alloying elements precipitate out of the Fe-phase as solute-rich phases (typically carbides). During this cooling, the FCC austenite transforms to body-centered-cubic (BCC) α-ferrite [7–9].

Compared to the annealed state, the higher strength and less ductile condition of steel is the hardened state. Hardening involves rapid (non-equilibrium) cooling of the steel from the austenitizing temperature. [2,7–10]. This rapid cooling is at a rate that does not allow diffusion of carbon to take place. Thus, preventing the FCC austenite from transforming to the BCC α-ferrite with carbides. Instead, a metastable body-centered-tetragonal (BCT) phase called martensite is formed. Martensite is a metastable phase that is held out of equilibrium by the supersaturation of alloying elements which were dissolved

into the austenite phase at higher temperature. Steel with martensitic structure is fully hardened [7–9].

Steel in the as-hardened condition remains extremely brittle. Brittle behavior of as-hardened steel is attributed to the internal stress and high density of dislocations produced during the diffusionless martensitic phase transformation [11]. The crystallographic strain present in martensite increases the materials strength; however, this crystallographic strain is deleterious to toughness. To maintain the strength and add ductility to the material, the as-hardened steel is tempered. Tempering allows a controlled amount of diffusion to take place. Time and temperature affect the amount of diffusion that occurs. As the tempering temperature increases, the steel will experience higher rates of diffusion and approach equilibrium more rapidly [12].

1.3. Microstructures of Hardenable Steel

The microstructure of hardenable steel changes predictably in response to heat treatment. The as-hardened microstructure of an alloyed steel, which is farthest from equilibrium, is dominated by lath-like martensite with minor bright regions of retained austenite and carbides. The lath martensite microstructure remains relatively unchanged until the martensite is restructured into tempered martensite. Fully tempered martensite is a microstructure of α-ferrite with dispersed fine-grained secondary carbides. Due to the precipitation of the fine-grained carbides, the α-ferrite is no longer super-saturated in carbon; thus, the lattice strain and dislocation density is reduced relative to martensite. The tempered martensite microstructure decreases the strength of the steel (compared to martensite) but improves the ductility of the steel. The microstructure of annealed steel, which is at equilibrium, has α-ferrite and carbides; this microstructure is coarser-grained compared to the as-hardened or fully tempered martensite microstructure [7–9].

Carbide forming elements that are common in tool steels and are pertinent to CPM® 3V in decreasing order of affinity are V > Mo > Cr > Fe [13–15]. Cr and Fe have similar carbide forming potential, so Cr-bearing carbides tend to also include Fe [7,10,16]. Stronger carbide forming elements such as V and Mo are desirable because they form carbides that remain stable during austenitization. The presence of carbides during austenitization is important to maintaining small austenite grains. Additionally, V-type carbides (VCs) are known to greatly improve the wear resistance of steels [17] Conversely, non-carbide forming elements stay within the Fe-phase throughout the heat treatment; Mn and Si are considered non-carbide forming elements [7,8].

2. Materials and Methods

The work that is outlined below was carried out at Montana Technological University (MTech). Machining of the tensile samples was done by a third-party machine shop. All other sample preparation and testing was carried out at MTech.

2.1. Bulk Composition

Bulk elemental analysis of the CPM® 3V steel was done using an AMETEK, SPECTRO MAXx LMM07 Arc/Spark Optical Emission Spectrometer (Arc/Spark OES). Prior to the analysis, calibration was performed using a Spectro RH 18/56 standard. Bulk composition analysis was completed on a section of the original round stock in the as-received condition. Three spots were analyzed; the average of the three analyses is reported in the composition table (Table 1).

2.2. Sample Preparation

2.2.1. Standard Test Specimen Machining

Eleven ASTM E8 standard tensile test specimens were machined from CPM® 3V 0.64″ diameter round stock in the annealed, unhardened condition. The tensile samples were cut to dimensions specified by ASTM E8 [18]: gauge diameter of 0.25″ and gauge length 1.25″ (e.g., $\geq$4 times the diameter; Figure 1). The ends of the samples were threaded with

5/8″ × 11 thread to facilitate the set up for the MTS Landmark tensile testing machine. SAE (Society of Automotive Engineers) Grade 8 bolts and couplers were used to secure the samples in the jaws of the tensile fixture to prevent the hardened CPM® 3V steel from deforming the jaws.

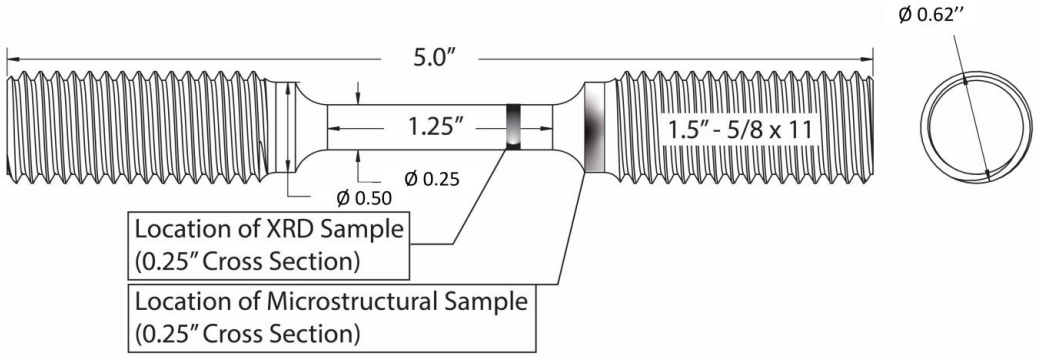

Figure 1. Drawing of the standard ASTM E8 tensile test specimen [18]. Highlighted areas show location of XRD and microstructural samples.

2.2.2. Heat Treating

The samples were heat treated in a box furnace under normal atmospheric conditions. Samples were coated in ATP-641 anti-scale coating to minimize oxidation during each step of the heat treatment. One sample was left in its untreated, annealed state (As-Received). The other ten samples were coated in the anti-scale coating and preheated in the furnace from room temperature to 800–840 °C at a rate of ~10 °C/min. Once the furnace reached this temperature, the samples were allowed to equalize in the furnace for 20 min. The samples were taken from the preheat and placed directly into the austenitizing furnace that was held at 1056 °C. After the samples were placed into the austenitizing furnace, the furnace was allowed to recover to 1056 °C and the samples were held at 1056 °C for 30 min to ensure the samples were fully heated. The samples of CPM® 3V were then quenched in air under natural convection following the austenitizing step. One of the hardened tensile specimens was kept in the as-hardened condition (As-Hardened).

Following the hardening step, the nine remaining samples were diversified in the tempering step (Figure 2). The anti-scale coating was reapplied, and the remaining tensile specimens were tempered at four temperatures. The different tempering temperatures were set at 450 °C (2 samples: 450A, 450B), 550 °C (3 samples: 550A, 550B, 550C), 650 °C (2 samples: 650A, 650B), and 700 °C (2 samples: 750A, 750B). The samples were triple tempered (as recommended by the manufacturer). During each tempering, the specimens were put into a furnace at their specified tempering temperature and held at that temperature for two hours each cycle. The samples were then removed from the furnace and placed on a refractory block to cool in air. After tempering, the samples were cleaned before tensile testing.

2.3. Mechanical Testing

2.3.1. ASTM E8 Tensile Testing

The tensile mechanical behavior was evaluated according to [18] using an MTS Landmark tensile fixture. The tensile fixture was equipped with a 55 kip load cell and all tests were done at room temperature. The strain rate could not be controlled directly, so a crosshead speed was set to 0.05″/min and the strain rate was verified using an extensometer that recorded the strain within the gauge length (Figure 1). The distance between pins on the extensometer was 1.143″. The stress data from the load cell and the strain data from the extensometer were collected at 100 Hz and then combined and reduced. Ultimate tensile strength (UTS) is defined as the maximum stress achieved during tensile failure. Yield strength was found using the 0.2% offset method. Tensile toughness (area under the

curve) was calculated [9]. Results were plotted in reference to the performance of each heat treatment. As-Received and As-Hardened tensile tests were not duplicated because they are not hardened and tempered samples and were not the focus of this investigation. The results are still reported for the sake of discussion, However, without additional tests, it should be noted that potential material irregularities and defects could have influenced the tensile behavior in these two treatments.

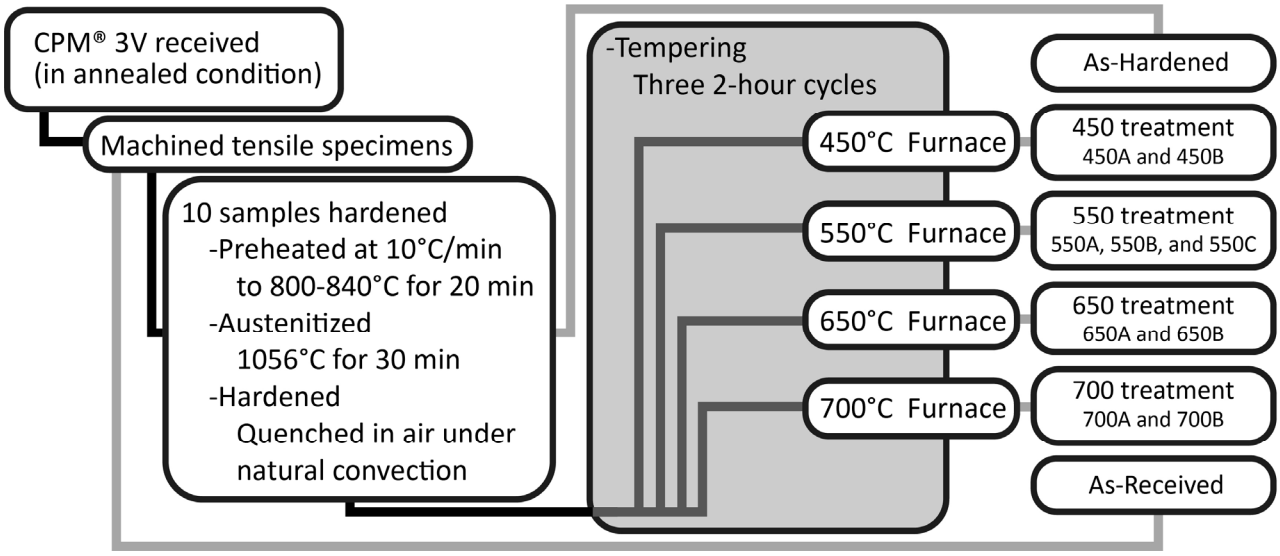

Figure 2. Flow chart showing the heat treatment steps. Tempering temperature was changed between sample sets.

2.3.2. Hardness Testing

Hardness of CPM® 3V was measured in HRC using a Mitutoyo HR-400 Rockwell hardness testing. Both the 0.5″ and 0.25″ cross sections were measured to ensure equivalent microstructural and thermal history along the gauge length (that underwent the tensile failure and was used for X-ray diffraction analysis, see below) and the threaded ends (that were used for microstructural observations, see below). Three tests that were within 2 HRC were recorded; an average of both cross sections was reported with standard deviation in Table 2.

Table 2. Results of the tensile test and Rockwell hardness (HRC).

Spec ID	HRC Hardness (Standard Deviation)	Max Stress: ksi (MPa)	Yield Stress: ksi (MPa)	% RA	AUC * (lbf/in2)	Avg. AUC
AR *	17.8 (0.61)	107 (738)	76 (524)	50.6	18539	
700A	32.2 (0.45)	147 (1013)	108 (745)	42.7	20281	20544
700B	32.2 (0.31)	150 (1034)	111 (765)	40.9	20806	
650A	34.1 (0.12)	167 (1151)	129 (889)	38.0	16749	17372
650B	34.8 (0.40)	159 (1096)	122 (841)	24.1	17995	
550A	58.6 (0.31)	332 (2289)	287 (1978)	20.4	17971	14660
550C	59.6 (0.25)	323 (2227)	274 (1889)	7.8	11349	
450A	60.4 (0.31)	324 (2227)	293 (2020)	1.6	4434	3471
450B	60.0 (0.10)	303 (2089)	291 (2006)	0.8	2508	
AH *	59.9 (0.21)	268 (1847)	201 (1386)	0.8	2206	

* AH: As-Hardened, AR: As-Received, AUC: Area Under Curve.

2.4. Analysis

2.4.1. Fractography

Micro-fractographic observations were used to investigate the mode of failure at appropriate scales. Micro-fractography of the fracture surfaces were observed on a TESCAN MIRA scanning electron microscope (SEM). The fracture surfaces were observed at the same magnification for all samples and the failure mode was interpreted as ductile or brittle.

2.4.2. Microstructural and Elemental Analysis

Microstructural investigations were performed at different magnification on both a Leica DMILM LED reflected light microscope and a TESCAN MIRA SEM equipped with an EDAX energy dispersion spectroscope (EDS). Sections of the standard tensile test specimen that were cut from the large 0.5″ ends of the standard tensile samples were mounted in phenolic using a LECO MX400 hot mounting press. Samples were prepared for etching using standard grinding and polishing methods. Villella's reagent was used to enhance the grain boundaries. In addition to micrographic analysis, EDS on the SEM was used to collect compositional information of the carbides present throughout the treatment. However, due to the small size of the carbides ($\leq$4µm), the carbide compositions were not well constrained and will not be discussed in this paper. The interested reader is referred to [19] regarding discussion of carbide composition analyses. In this paper, carbides are qualitatively named using the dominant alloy element in the carbide as presented in [19].

2.4.3. X-ray Diffraction

Crystallographic trends were investigated with a Rigaku Ultima IV X-Ray diffractometer (X-ray diffraction; XRD). XRD analyses were completed on slices of the 0.25″ gauge length. The slices were placed on a stationary stage and scans were completed from $2\theta = 20^\circ$ to 140°. The X-ray source was a cobalt tube with a Ka1 = 1.788996, Ka2 = 1.792835 equipped with an Fe filter. Peak matching was aided by MDI Jade software package. Due to the overwhelming peak intensity from the Fe matrix in the steel, the carbide identification was limited, and volume percentages were not able to be calculated.

3. Results and Discussion

The main goal of this study was to establish trends in the mechanical behavior of CPM® 3V among different tempering temperatures and correlate the mechanical behavior with observed microstructures. Microstructural, fractographic, and compositional analyses were conducted to help explain the similarities and differences in mechanical behavior (e.g., tensile strength, hardness) of the various heat treatments. The differences among the various heat treatments produced two broad groups: a low temperature group (As-Hardened, 450 °C, 550 °C) and a high temperature group (650 °C, 700 °C, As-Received). These groups will be referred to along with individual heat treatments.

3.1. Mechanical Behavior

The results for the tensile testing (Figure 3) and Rockwell hardness (HRC) are tabulated in Table 2. Four basic mechanical parameters were used to describe the mechanical properties in tensile performance: ultimate tensile strength (UTS), yield strength (YS), and percent reduction of area (% RA).

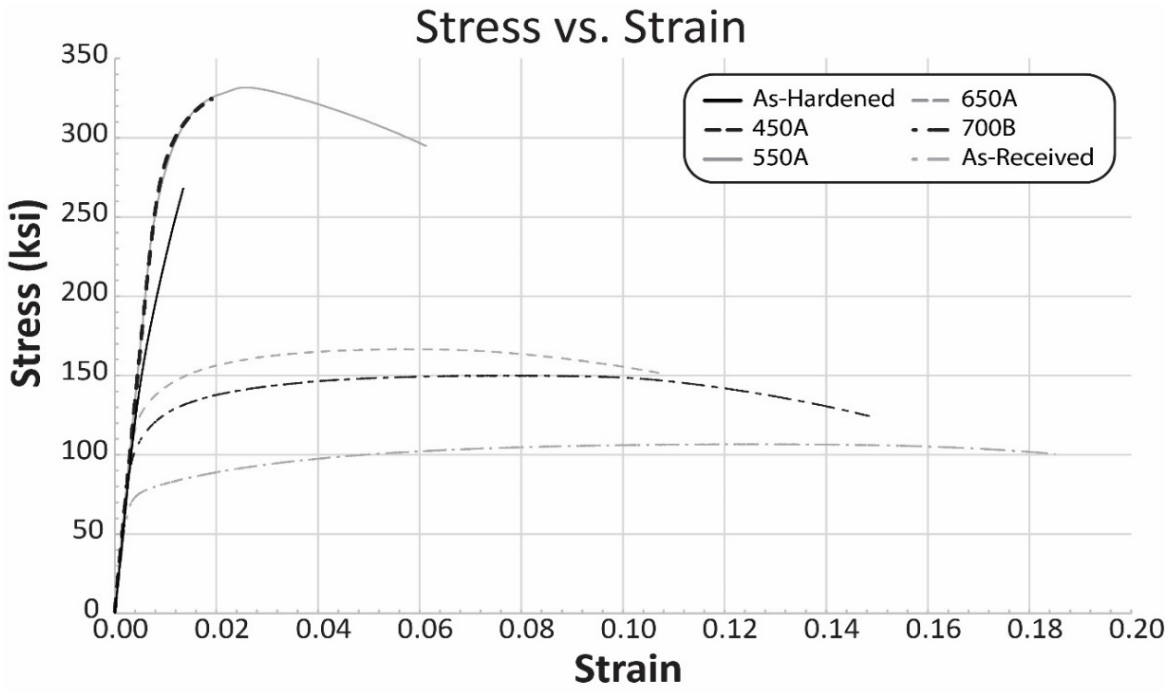

Figure 3. Stress vs. strain graph for representative tests. Note: As-Hardened and As-Received tensile tests were not duplicated.

3.1.1. Strength

The stress stain curves seen in Figure 3 illustrate the tensile performance of CPM® 3V for each tempering temperature. Both yield strength (YS) and ultimate tensile strength (UTS) trend together throughout the sample set. The following results and discussion will focus on the UTS, but the trends generally apply to the YS as well.

The As-Hardened samples performed as expected in the tensile testing with a stress strain curve that is representative of a perfectly brittle material that did not experience any plastic deformation and therefore, had the smallest area under the curve (Figure 3). Increasing tempering temperature from As-Hardened to 450 °C and 550 °C tempering, results in an increase in the plastic portion (horizontal section) of the stress strain curve and an increase in the UTS. The As-Hardened samples had a UTS of ~268 ksi, the 450 °C tempered samples averaged ~313 ksi, while the maximum UTS for all samples was ~327 ksi at 550 °C. Above the 550 °C tempering, there is ~50% decrease in the UTS and ~200% increase in the plasticity of CPM® 3V. As the tempering temperature increased from 650 °C to 700 °C and As-Received (annealed), the CPM® 3V became weaker and more ductile. The 650 °C sample had a UTS of ~162 ksi, the 750 °C tempered samples averaged 148 ksi, and the As-Hardened sample had the lowest UTS of all samples measuring 106 ksi. The As-Received sample had the highest ductility of the samples. The 700 °C tempering treatment, however, had comparable plasticity to the As-Received sample at a higher strength.

The increase in the tensile strength going from As-Hardened to 450 °C tempering is likely due to reduction of retained austenite in the microstructure; retained austenite was only identifiable using reflected light. The increase in strength going from 450 °C to 550 °C tempering could be explained by recovery in the hardened martensite as tempering reduced the dislocation density [20]. Reduced dislocation density would allow the CPM® 3V to achieve a higher UTS compared to the 450 °C tempered samples due to a decrease in stored lattice strain [8,9]. The large shift in the mechanical behavior between 550 °C and 650°C tempering is indicative of a change in the material's structure between these temperatures (discussed below). The continued reduction in strength and increase in ductility from 650 °C tempering to 700 °C tempering is likely due to the grain growth as the temperature is raised.

3.1.2. Ductility

In contrast to the strength of the material, the ductility did not have a maximum, instead there was an increase in ductility proportional to tempering temperature. The ductility is low in the As-Hardened sample with a % RA of 0.8. Ductility slowly increased in the low temperature samples from an average % RA of 1.2 in the 450 °C tempered samples to an average % RA of 14.1 in the 550 °C tempered samples. However, the individual 550 °C tempered samples had a wide range of values with the 550A and 550C having % RA of 20.4% and 7.8%, respectively. The ductility jumped to an average % RA of 31 in the 650 °C tempered samples and then changed more slowly to an average % RA of 41.8 and 50.6 in the 700 °C samples and As-Received, respectively. The largest increase in ductility was at the same tempering temperatures that the decrease in strength was documented (between 550 °C and 650 °C) suggesting they likely are caused by the same change in the steel.

3.1.3. Hardness

Hardness is a measurement of a material's resistance to plastic deformation. Hardness relates to UTS in many materials and is a common tool for quality control of alloys with well understood properties. CPM® 3V showed very little change in its hardness when tempered at ≤550 °C. The hardness of the low temperature group was ≥58 HRC and was very constrained—only varying 1.8 HRC (very close to the 1.5 HRC error of the Mitutoyo HR-400). There was a significant drop (almost 50%) in hardness at the 650 °C tempering treatment. Hardness continued to decrease with increased temperature, albeit at a slower rate than the drop from 550 °C to 650 °C. All the high-temperature treatments have a much lower hardness than the low-temperature treatments (≤30 HRC for high temperature samples versus ≥58 HRC for low temperature samples; Table 2). The hardness of the samples in increasing order of hardness is: As-Received < 700 °C < 650 °C < 550 °C < As-Hardened < 450 °C.

3.2. Microscopic Observations

3.2.1. As-Hardened

The As-Hardened microstructure was dominated by lath-like as-quenched martensite (Figure 4a,b). The martensite in the As-Hardened sample contained the brightest regions within the lath-like microstructure that was optically interpreted to be retained austenite (Figure 4a). Primary carbides were seen throughout the sample typically at the boundaries of the martensite islands (Figure 4b). The primary carbides are thought to be a mix of M_7C_3 Cr-rich carbides and MC V-type carbides (see crystallography section below and [19]). VCs have exceptional high temperature stability and are typical primary carbides in tool steels. The presence of VCs is desirable to increase wear resistance in steel due to VCs high hardness [14,17]. In addition to M_7C_3 and MC carbides, M_3C and M_6C carbides [13,15] may also be present based on a low metal:carbon ratio identified in a few samples [19]. Differences in the primary carbides in the As-Hardened, 450 °C, 550 °C, 650 °C, and 700 °C—tempered samples were not able to be differentiated and will be referred to as mixed carbides in the following sample summaries.

The fractography of the As-Hardened sample was characterized by flat regions and indicated brittle failure with flat fracture geometry devoid of any shear lip (Figure 4c,d). This was expected from the perfectly brittle As-Hardened stress–strain curve discussed above. The lack of ductile features in the fractography was also consistent with a % RA of <1% (0.8% RA). Brittle behavior in the As-Hardened condition was attributed to high dislocation density and the associated internal stress in non-tempered, hardened steels.

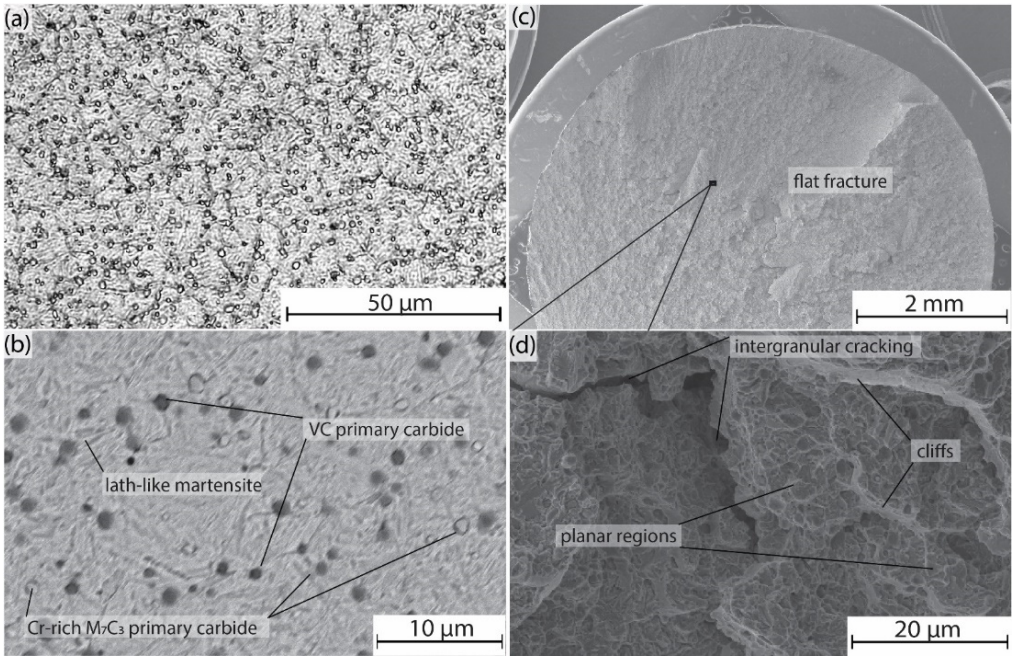

Figure 4. (**a**) Reflected light image of As-Hardened sample. Bright regions in the lath-like background are interpreted to be retained austenite. (**b**) Backscatter electron image highlighting the lath-like as-quenched martensite and mixed primary carbides. (**c**) Wide-field secondary electron image of fracture surface highlighting the flat brittle fracture mode. (**d**) Small-scale secondary electron image highlighting brittle features.

3.2.2. 450 °C Tempering

Similar to the As-Hardened sample, the microstructure of the 450 °C was dominated by lath-like as-quenched martensite (no image shown). The white retained austenite areas that were seen in the As-Hardened samples were less noticeable in the 450 °C sample. The carbides present in the 450 °C material were the same mixed carbides seen in the As-Hardened sample [19]. The fracture surface of the 450 °C samples was dominated by flat features. Overall, the 450 °C and As-Hardened microscopic observations where remarkably similar even though their mechanical behavior showed a slight increase in ductility and % RA. Multiple tempering cycles at 450 °C may have reduced the retained austenite and allowed a small amount of crystalline recovery in the 450 °C material which allowed it to absorb more tensile energy before failure. Reduced retained austenite was supported by the 450 °C sample having slightly less noticeable bright regions in the lath like martensite compared to the As-Hardened sample.

3.2.3. 550 °C Tempering

Tempering CPM® 3V at 550 °C had a relatively small effect on the microstructure compared to the 450 °C samples, even though there was significant increase in strength and % RA of the steel. The microstructure of the 550 °C was dominated by lath-like as-quenched martensite (Figure 5a,b). The martensitic matrix in the 550 °C sample was a more uniform grey color (Figure 5a) showing a further reduction in the retained austenite compared to the As-Hardened and 450 °C samples. The carbides in the 550 °C material were similar to the mixed carbides from the previous samples [19].

The micro-fractography in the 550 °C samples had a mix of brittle and ductile features: there was brittle flat regions and cliffs, and ductile honeycomb structure with ductile dimples and ridges. The macro-view of the fracture was mostly flat; however, one of the 550 °C samples displayed shear lips indicating a more ductile cup and cone failure. The multiple tempering cycles at 550 °C versus 450 °C likely reduced more of the retained austenite and increased crystalline recovery in comparison to the 450 °C samples. This

would have allowed the material to absorb significant energy while maintaining high strength; this is consistent with the 550 °C samples having the maximum UTS before they finally necked to failure (Figure 3).

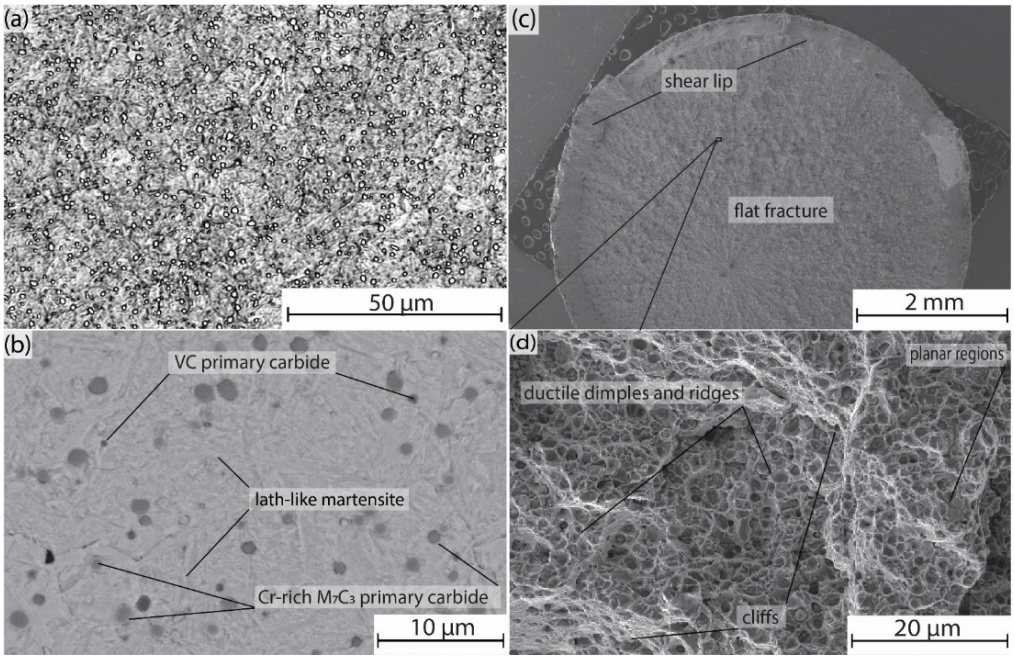

Figure 5. (**a**) Reflected light image of 550 °C sample. Bright spots, interpreted as retained austenite, are fewer than those seen in the As-Hardened sample. (**b**) Backscatter electron image highlighting the lath-like as-quenched martensite and mixed primary carbides. (**c**) Wide-field secondary SEM image of fracture surface highlighting a shear lip with flat fracture in central region. (**d**) Small-scale secondary electron image highlighting brittle cliffs and planar regions with ductile dimples and ridges.

3.2.4. 650 °C Tempering

The microstructure of the 650 °C samples (no image shown) had a broad restructuring with tempered martensite replacing the as-quenched martensite. The primary carbides in the material did not show any change at the 650 °C tempering and are thought to be the same mixed carbides seen in the previous samples [19]. However, at 650 °C secondary carbides can be seen as very fine, bright spots in the tempered martensite similar to what is shown in the 700 °C sample (Figure 6b). Based on the texture, morphology, location, and brightness of these fine-grained phases they are likely $M_{23}C_6$ Cr-rich carbides. Studies by [21] and [22] found that tempered Cr-rich tool steels form two common Cr-carbides: M_7C_3 and $M_{23}C_6$. Generally, M_7C_3 Cr-rich carbides form prior to the $M_{23}C_6$ carbides. Since M_7C_3 carbides are interpreted to be part of the primary carbides [19], the smaller secondary carbides that appear in the 650 °C and 700 °C treatments are likely $M_{23}C_6$ Cr-rich carbides. Furthermore, [23] and [16] found that the Cr defuses rapidly out of the Fe-phase above ~500 °C and forms secondary Cr-carbides. Thus, the precipitation of the secondary carbides at temperatures > 550 °C for CPM® 3V is consistent with [23] and [16]; the higher percentage of Mo in CPM® 3V may be raising the tempering temperature at which the secondary carbides are observed.

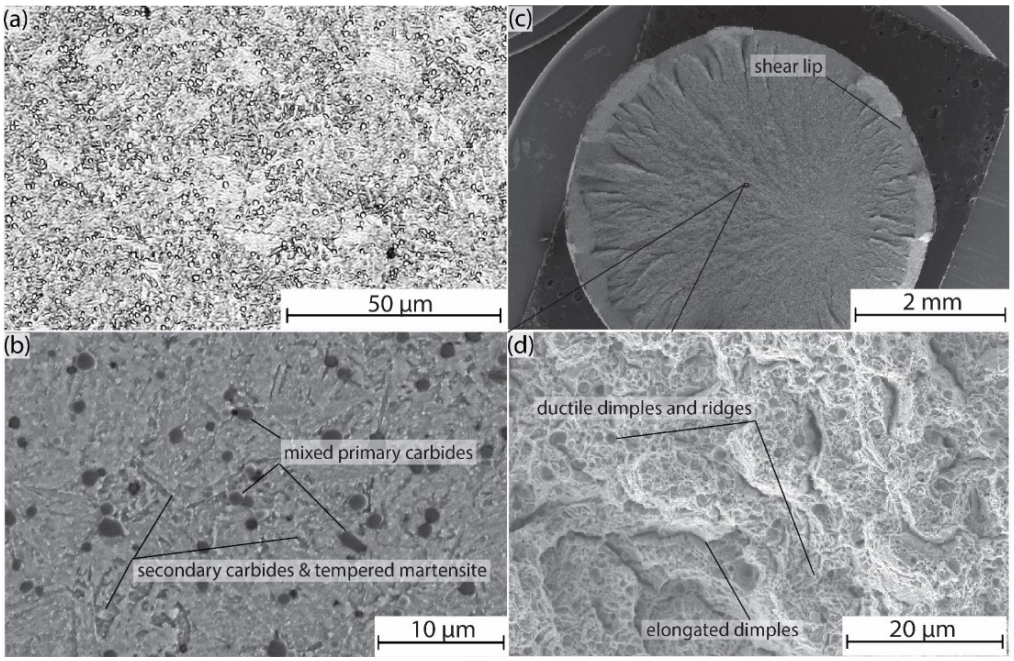

Figure 6. (**a**) Reflected light image of the 700 °C sample. Bright background textures contain tempered martensite which differs from the lath-like as-quenched martensite in the low temperature samples (Figures 3 and 4). (**b**) Backscatter electron image highlighting the occurrence of tempered martensite and secondary carbides. (**c**) Wide-field secondary image of fracture surface highlighting shear lip. (**d**) Small-scale secondary electron image highlighting ductile dimples and ridges showing a ductile mode of failure.

The fractography of the 650 °C samples were dominated by ductile features, with micro-fractography showing honeycomb structure and ductile dimples and ridges. The macro view of the fracture was not as flat as the lower temperature samples and the 650 °C samples displayed shear lips indicative of a more ductile cup and cone failure. The increase in ductility is likely explained by the loss of tetragonality as the as-quenched martensite transitions to tempered martensite. As the as-quenched martensite transitions to tempered martensite, there is precipitation of secondary carbides. Precipitation of carbides lowers the amount of alloy elements dissolved into the matrix, which ultimately reduces stored energy (strain) in the lattice of the Fe-matrix [22,24].

3.2.5. 700 °C Tempering

Similar to the 650 °C samples, the microstructure of the 700 °C contained tempered martensite replacing the as-quenched martensite (Figure 6a,b). The primary carbides in the material did not show any change [19]. However, there were more secondary carbides, seen as very fine bright spots within the tempered martensite, compared to the 650 °C samples. These secondary carbides are likely to be the continued growth of the $M_{23}C_6$ Cr-rich carbides. The fractography of the 700 °C samples were dominated by ductile features (Figure 6c,d). The micro-fractography showed honeycomb structure and ductile dimples and ridges (Figure 6d). The macro view of the fracture was similar to the 650 °C samples: it was not flat like the lower temperature samples but displayed shear lips indicative of ductile cup and cone failure (Figure 6c). The increased ductility in the 700 °C samples was likely caused by further precipitation of the secondary carbides, as well as potential grain growth in the tempered martensite. However, due to the complexity of the microstructures and the fine grain size, grain size analysis could not be conducted during this study. Therefore, grain growth between the 650 °C and 700 °C samples is conjectured at this point.

3.2.6. As-Received

The material that was received in the annealed condition is discussed last because it represents CPM® 3V after reaching equilibrium. The microstructure of the As-Received sample has a matrix of α-ferrite with mixed carbides. The carbides were all of similar size in this sample and could not be denoted as primary or secondary. The carbides present in the annealed CPM® 3V are thought to be the M_7C_3 Cr-rich carbides and MC V-type carbides, as seen in the other samples [19]. In addition to the M_7C_3 and MC carbides, there are bright white carbides (Figure 7). The bright white carbides are suggested to be further growth of the bright white carbides that were newly precipitated at the grain boundaries of the 650 °C and 700 °C treatments. These bright white carbides are thought to be $M_{23}C_6$ Cr-rich carbides. The fracture surface of the As-Received sample was characteristic of ductile failure with ductile dimples and ridges, irregular fracture surfaces, and a shear lip indicating cup and cone failure. Overall, the equilibrium cooling allowed the As-Received sample to have more complete diffusion of solute atoms (C, Cr, Mo, and V) out of the Fe-phase, leading to more abundant carbides present—notably the $M_{23}C_6$ carbides. The large grain size of the α-ferrite and the lack of strain induced by solute atoms allowed the α-ferrite in the As-Received sample to be more ductile.

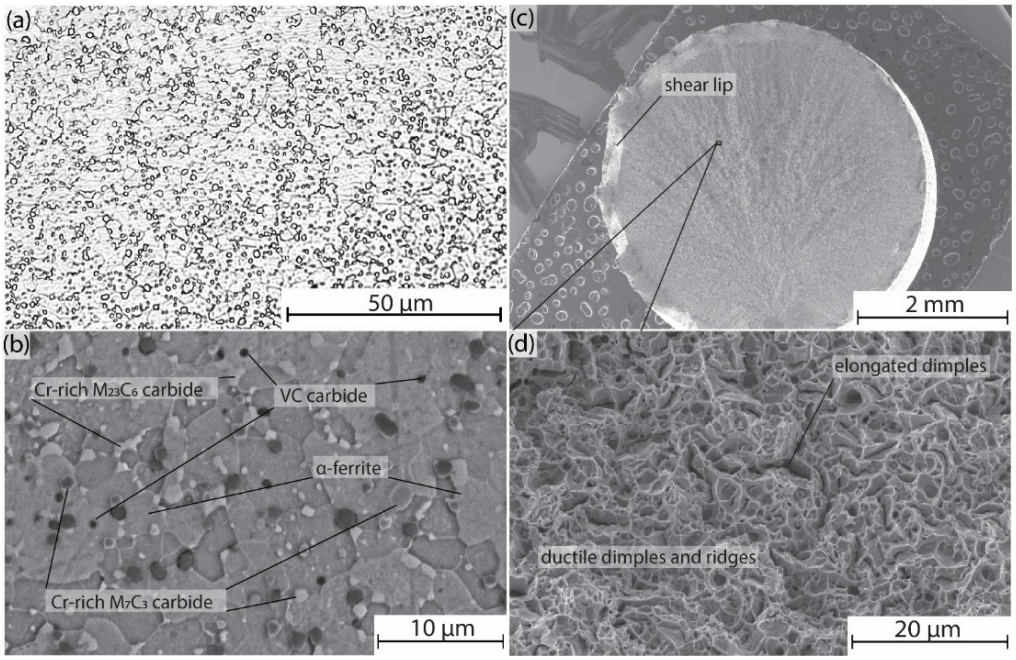

Figure 7. (**a**) Reflected light image of the As-Received sample. Background is featureless α-ferrite. (**b**) Backscatter electron image highlighting α-ferrite, mixed carbides, and bright white Cr-rich $M_{23}C_6$ carbides along grain boundaries. (**c**) Wide-field secondary image of the fracture surface highlighting a shear lip. (**d**) Small-scale secondary electron image with ductile dimples and ridges showing ductile mode of failure.

3.3. Crystallographic Trends

The only carbide phase identified using XRD was a cubic V-type MC carbide. In addition to the V-type carbide, there were broad peaks in the XRD spectra (marked by circles in Figure 8) that were recognized by the MDI Jade software. However, these peaks were extremely low intensity and diffuse, resulting in an inability to accurately identify a specific crystallographic phase. These low intensity peaks are likely other mixed carbide phases.

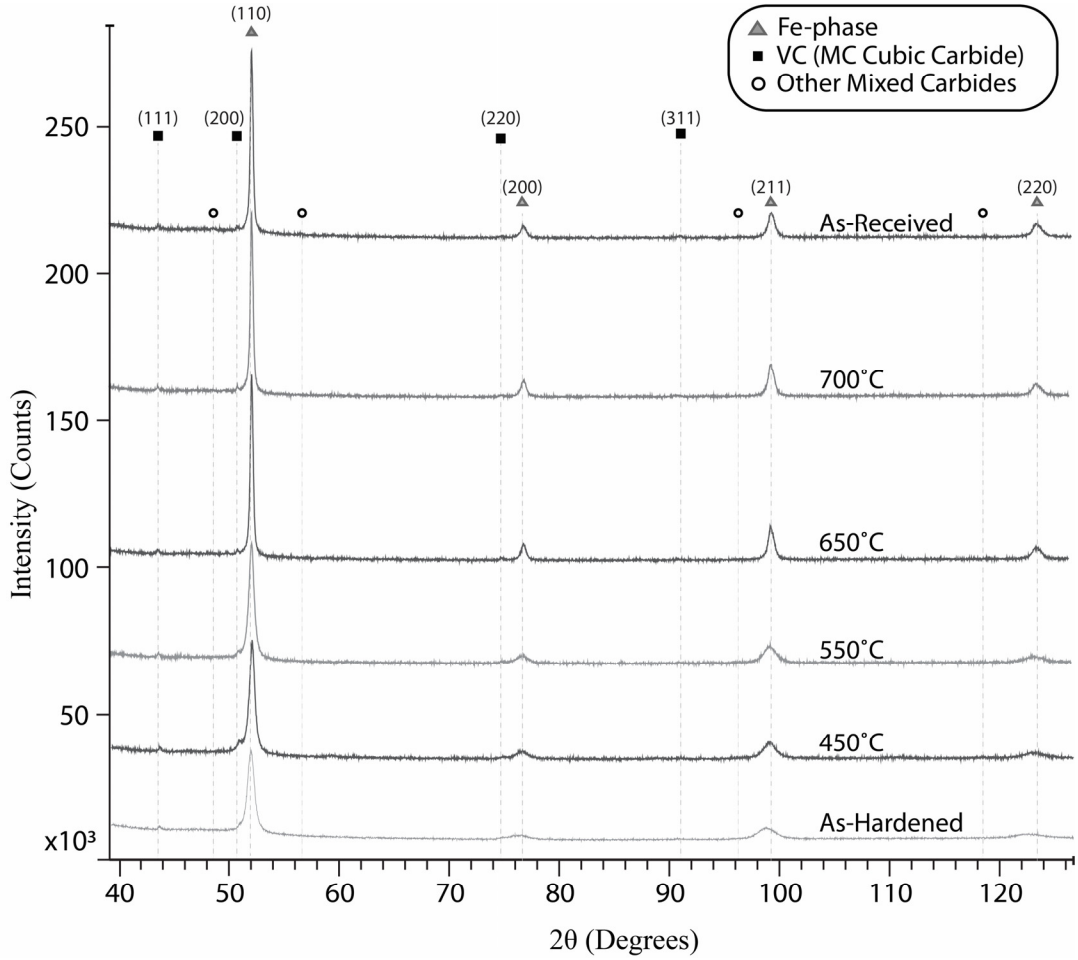

Figure 8. Offset plot of the XRD fractogram at each level of the treatment. Crystallographic peaks and Miller indices were identified by MDI software. Iron peaks narrow and increase in intensity most notably after 650 °C.

Even though it was not possible to identify the mixed carbides using XRD, there were changes in the shape of the XRD Fe-phase peaks. The As-Hardened, 450 °C, and 550 °C treatments have nearly identical Fe-phase peak intensity and shape (Figure 8). Whereas Fe-phase peaks in the 650 °C and 700 °C treatments have a higher intensity and narrower peak width than the low temperature treatments. Narrowing of peak widths and increasing intensity indicates that the crystal lattice of the Fe-phase becomes more symmetrical and less strained with increasing tempering temperature.

The broader Fe-phase peaks are consistent with martensite being the primary structure in the low temperature samples. Martensite is highly strained due to the supersaturation of carbon trapped within the crystal structure. Martensite is classified as BCT; however, the strain of the crystal structure in the c-axis is dependent on (proportional to) the amount of carbon that is dissolved in the Fe phase during austenitization [25–28]. Heterogeneity in the carbon distribution could cause variable elongation in the martensite lattice structure and result in broader Fe-phase peaks in the lower temperature samples [29,30]. The sharpening of the Fe peaks above 550 °C likely represents the loss of tetragonality as martensite (BCT) becomes tempered martensite (α-ferrite BCC). During this transition, the carbon is allowed to defuse out of the Fe-phase and form secondary carbides. The change in peak intensity and width and the interpretation of the martensite becoming more symmetric at temperatures > 550 °C aligns with the first microstructural observation of tempered martensite and secondary carbides at 650 °C.

3.4. Relationship of Process, Microstructure, and Mechanical Behavior

The process (e.g., tempering) by which a steel component is produced drives the microstructures which form within the steel and ultimately dictate the final mechanical behavior of the steel. To highlight how microstructure affected the mechanical behavior in CPM® 3V, the strength, degree of ductility, microstructural, and fractography trends are summarized together. Before this discussion, it is important to be aware of the classical inverse relationship between strength and ductility. In this study, the exceptions to the inverse strength-ductility relationship are the As-Hardened, 450 °C, and 550 °C tempering treatments. Throughout these low temperature treatments, both the ductility and the strength appear to increase together with temperature. This behavior is likely caused by partial tempering experienced by the low temperature samples. Low temperature ($\leq$550 °C) tempering likely reduces both the stored internal stress and the dislocations trapped in the steel during the austenite to martensite phase transition when hardening [20]. When CPM® 3V was tempered above 550 °C, the internal stress is likely completely released. Therefore, the >550 °C tempering treatments have the expected relationship in which strength decreases as ductility increased [7–9].

Throughout the experiments there is a marked change in the material when it is tempered above 550 °C. There is a consistent trend in the crystallography (XRD), microstructural, and the mechanical properties of the material. The shape of the peaks changed dramatically between 550 °C and 650 °C (Figure 8) indicating the martensite was losing its tetragonality [30]. Microstructurally, the textures observed in the Fe-phase change at tempering temperatures above 550 °C. The martensite matrix changed from as-quenched, lath-like martensite at tempering temperature of 550 °C and below to a martensite matrix that included tempered martensite with precipitated secondary carbides at tempering temperatures of 650 °C and above (Figures 4 and 5). Additionally, the samples tempered at and below 550 °C had higher strength while mechanical strength was greatly reduced in the $\geq$650 °C samples. Overall, the loss of tetragonality as martensite goes to tempered martensite, and the precipitation of carbides which lower the alloy elements dissolved into the matrix, would both reduce stored energy (strain) in the lattice of the Fe matrix [21,23]. This strain reduction in the lattice would allow dislocations to move more easily and lead to increased ductility and decreased strength [8]. This is consistent with the more ductile failure observed in the high temperature samples ($\geq$650 °C).

The dominantly elastic strain exhibited by the low temperature treatments in their stress–strain curve is consistent with the brittle features observed in fractography. The $\leq$ 450 °C samples have only brittle features in the fractography and have stress–strain curves that are dominated by elastic strain. There is a mixture of brittle and ductile features in the $\geq$550 °C treatments. These treatments have flat, faceted features on the primary fracture surface while still having a shear lip; this indicates some cup-and-cone geometry diagnostic of ductility during failure (Figure 5). Consistent with the fractography, the 550 °C treatments experienced significant elastic strain but failed once experiencing some degree of plastic strain. The slight increase in ductility at 550 °C may be due to small unobservable portions of the martensite matrix beginning to form tempered martensite. Another possible explanation is that the martensite in the 550 °C samples had the lowest dislocation density due to crystal recovery during tempering and therefore, displayed some ductile behavior without a loss of tetragonality in the martensite [20,29]. The latter explanation would be supported by the fact that the XRD of the 550 °C samples did not appear to have sharper peaks than the 450 °C samples. The broader peaks indicate that the 550 °C samples do not contain very much tempered martensite relative to the other low temperature samples.

Higher ductility is seen in the high temperature treatments (650 °C, 700 °C, and As-Received) compared to the low temperature treatments (As-Hardened, 450 °C, and 550 °C). The high temperature fractography shows significant necking on the standard test specimens as well as prominent shear lips that is indicative of cup and cone fracture geometry. Likewise, all the high temperature stress–strain curves show large plastic regions

in their curve. The ductile behavior of the high temperature samples can be correlated to the presence of the tempered martensite in their microstructure.

Overall, for the heat treatments tested in this study, the 550 °C tempering had high hardness with sufficient ductility, making it optimal for high strength applications of CPM® 3V. The results of this investigation are specific to a 1056 °C austenitization treatment, air-quenching, and triple tempering for two hours each cycle (Figure 2). Changing the heat treatment parameters would alter the microstructure and mechanical behavior of the steel [1,7–9].

3.5. CPM® 3V Mechanical Behavior Comparison with Other Steels

Prior to optimizing CPM® 3V for new applications, it is useful to understand the similarities and differences in tempering response CPM® 3V steel has relative to commonly used steels. Figure 9 is a graph of CPM® 3V hardness response to variable tempering temperature compared to the tempering response of 1080, 4140, and H11 in the same temperature range. Hardness data for 1080, 4140, and H11 sourced from [8]. Compositions are listed in Table 3. The 1080 steel is a plain carbon steel that contains similar concentrations of carbon as CPM® 3V but does not have any additional alloy elements. Both 4140 and H11 are high-strength tool steels similar to CPM® 3V. However, 4140 is a low-alloy tool steel compared to the high-alloy compositions of both CPM® 3V and H11. H11 and CPM® 3V are both high-strength, high alloy steels, but H11 has less C, Cr, and V compared to CPM® 3V.

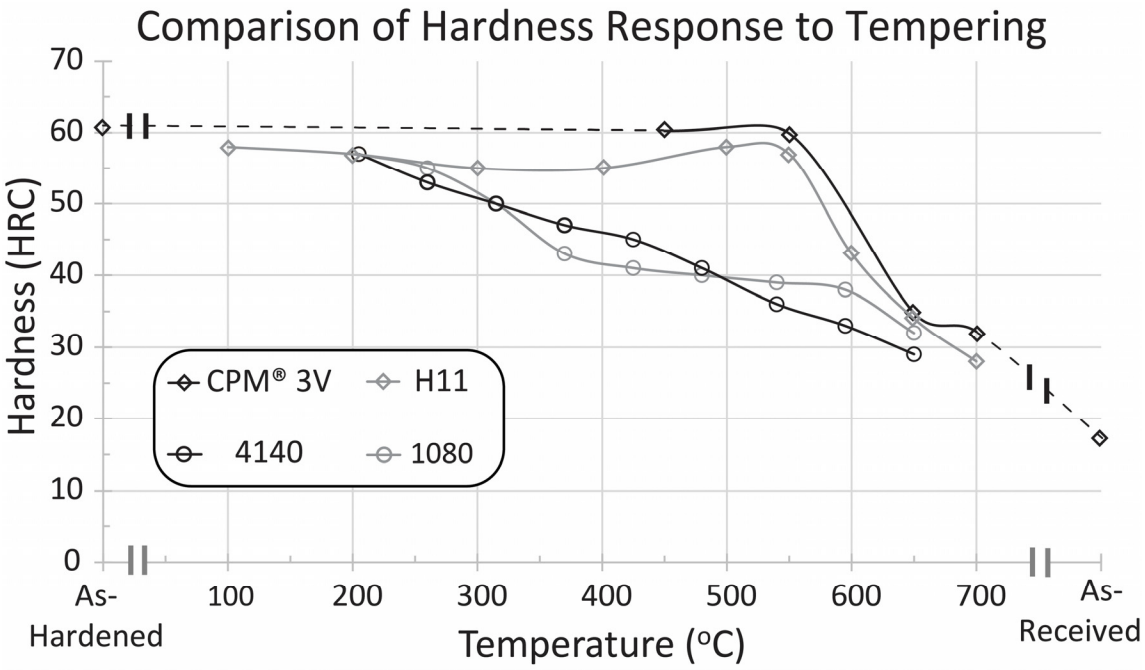

Figure 9. Comparison of HRC vs. tempering temperature response of CPM® 3V, H11, 4140, and 1080 steels. CPM® 3V hardness data is from this study; 1080, 4140, H11 hardness data is from [8].

Table 3. Composition of CPM® 3V measured using Arc/Spark OES. H11, 4140, 1080 compositions for tempering response comparison; compositions from published literature [31–33].

Steel Alloy	C	Si	Mn	Cr	Mo	V	P	S	Balance of Fe
CPM® 3V	0.71	0.84	0.38	7.81	1.32	2.53	0.0115	0.0138	86.38
1080	0.80	0.30	0.75	0.10	0.03	-	<0.0350	<0.0500	98.35
4140	0.43	0.19	0.90	0.98	0.18	-	<0.0350	<0.0500	97.24
H11	0.40	0.90	-	5.00	1.30	0.50	0.0150	0.0150	91.87

The hardness of 1080 decreases from 200 to 650 °C (Figure 9); there is a pronounced dip in hardness above 300 °C. The 4140 steel has a similar decrease in hardness with tempering temperature as 1080; however, the slope is more constant and does not have the pronounced dip above 300 °C. Additionally, the minimum hardness of 4140 is lower than that of 1080. H11 shows very different hardness-temperatures trends from 1080 and 4140. At low tempering temperature (between 100 °C and ~350 °C), there is only a very slight decrease in hardness. A secondary hardening response is seen in H11 between 400 °C and 550 °C, before the alloy shows a precipitous drop in hardness between 550 °C and 650 °C. In CPM® 3V, the hardness values at each treatment produce a curve that is very similar to that of H11 (Figure 9). The similarities in the tempering response between CPM® 3V and H11 suggests that their microstructure and mechanical behavior may also be similar within this temperature range.

However, it is important to note that there were sections of the CPM® 3V tempering response curve that did not have data and may not match H11. For example, the hardness of H11 dips between 100 °C and 350 °C. CPM® 3V was not tempered at temperatures < 450 °C so it is not possible to know if there is a similar secondary hardening behavior in CPM® 3V. However, it is common for high-speed tool steels to retain significant amounts of austenite in the as-hardened microstructure. During low temperature tempering, the amount of retained austenite will be reduced, subsequently increasing hardness. This process typically requires multiple tempering treatments in H11 [33]. As a similar tool steel, CPM® 3V may behave similarly. Possible evidence supporting retained austenite in CPM® 3V is the change in slope of the As-Hardened stress–strain curve at ~150 ksi compared to the 450 °C and 550 °C stress–strain curves. This change in slope could be caused by non-uniform yielding in the material due to weaker retained austenite. However, additional phase identification and tensile testing would be needed for confirmation.

4. Conclusions

The tempering response of CPM® 3V was investigated through the following tempering temperatures: As-Hardened (no tempering), 450 °C, 550 °C, 650 °C, 700 °C-Tempered, and As-Received (fully annealed). Tensile testing, hardness testing, reflected-light microscopy, SEM microscopy, and XRD crystallographic analysis were utilized to characterize the tempering, microstructure, and property relationship in CPM® 3V. The following conclusions were found:

1. Primary carbides did not appear to change among tempering treatments;
2. 550 °C is the optimal tempering temperature for high strength applications;
3. CPM® 3V steel tempered at $\geq$650° C contains tempered martensite with secondary carbides and results in a ~50% decrease in strength and a ~200% increase in ductility relative to the 550 °C treatment;
4. The CPM® 3V tempering response is similar to the industrially used steel H11.

Author Contributions: Methodology, S.A.C.H.; Validation, S.V.; Formal analysis, S.A.C.H.; Investigation, S.A.C.H.; Writing – original draft, S.A.C.H.; Writing – review & editing, S.V.; Visualization, S.A.C.H.; Supervision, S.V.; Project administration, S.V. All authors have read and agreed to the published version of the manuscript.

Funding: This research received no external funding.

Data Availability Statement: The data presented in this study are available within the article and in reference [19].

Acknowledgments: I would like to acknowledge and thank Gary Wyss, Cristina Stefanescu, and Cody Hennessy at MTech for their assistance with the SEM, XRD, Arc/Spark OES, and mechanical testing.

Conflicts of Interest: The authors declare no conflict of interest.

References

1. Crucible Selector—CPM®3V. Available online: https://www.crucible.com/eselector/prodbyapp/tooldie/cpm3vt.html (accessed on 24 March 2022).
2. Canale, L.C.; Albano, L.; Totten, G.E.; Meekisho, L. Hardenability of steel. *Compr. Mater. Process.* **2014**, *12*, 39–97.
3. Olevsky, E.A. Theory of sintering: From discrete to continuum. *Mater. Sci. Eng. R Rep.* **1998**, *23*, 41–100. [CrossRef]
4. Boccalini, M.; Goldenstein, H. Solidification of high speed steels. *Int. Mater. Rev.* **2001**, *46*, 92–115. [CrossRef]
5. Song, J.; Gelin, J.C.; Barriere, T.; Liu, B. Experiments and numerical modelling of solid state sintering for 316L stainless steel components. *J. Mater. Process. Technol.* **2006**, *177*, 352–355. [CrossRef]
6. Benedetti, M.; Torresani, E.; Leoni, M.; Fontanari, V.; Bandini, M.; Pederzolli, C.; Potrich, C. The effect of post-sintering treatments on the fatigue and biological behavior of Ti-6Al-4V ELI parts made by selective laser melting. *J. Mech. Behav. Biomed. Mater.* **2017**, *71*, 295–306. [CrossRef] [PubMed]
7. Vander Voort, G.F. *Metallography and Microstructures*; ASM International: Materials Park, OH, USA, 2004; Volume 9.
8. Dossett, J.L.; Totten, G.E. *Heat Treating*; ASM International: Materials Park, OH, USA, 1991; Volume 4.
9. Callister, W.D.; Rethwisch, D.G. *Fundamentals of Materials Science and Engineering*; Wiley: London, UK, 2000.
10. Purdy, G.R.; Brechet, Y.J. A solute drag treatment of the effects of alloying elements on the rate of the proeutectoid ferrite transformation in steels. *Acta Metall. Mater.* **1995**, *43*, 3763–3774. [CrossRef]
11. Thelning, K.E. Dimensional changes during hardening and tempering. In *Steel and its Heat Treatment*, 2nd ed.; Butterworth-Heinemann: Oxford, UK, 1984.
12. Laidler, K.J. The development of the Arrhenius equation. *J. Chem. Educ.* **1984**, *61*, 494–498. [CrossRef]
13. Luo, Y.; Guo, H.; Guo, J. Effect of cooling rate on the transformation characteristics and precipitation behaviour of carbides in AISI M42 high-speed steel. *Ironmak. Steelmak.* **2018**, *46*, 698–704. [CrossRef]
14. Bourithis, L.; Papadimitriou, G.D.; Sideris, J. Comparison of wear properties of tool steels AISI D2 and O1 with the same hardness. *Tribol. Int.* **2006**, *39*, 479–489. [CrossRef]
15. Hetzner, D.W.; Van Geertruyden, W. Crystallography and metallography of carbides in high alloy steels. *Mater. Charact.* **2008**, *59*, 825–841. [CrossRef]
16. Horovitz, M.B.; Beneduce Neto, F.; Garbogini, A.; Tschiptschin, A.P. Nitrogen bearing martensitic stainless steels: Microstructure and properties. *ISIJ Int.* **1996**, *36*, 840–845. [CrossRef]
17. Wei, S.; Zhu, J.; Xu, L. Research on wear resistance of high speed steel with high vanadium content. *Mater. Sci. Eng. A* **2005**, *404*, 138–145. [CrossRef]
18. *ASTM E8/E8M-16a*; Standard Test Methods for Tension Testing of Metallic Materials. ASTM International: West Conshohocken, PA, USA, 2016.
19. Hanson, S.A.C. The Tempering Response of CPM®3v Tool Steel Investigated through Tensile Testing and Microstructural Observations. Master's Thesis, Montana Technological University, Butte, MT, USA, May 2022.
20. Kennett, S.C.; Krauss, G.; Findley, K.O. Prior austenite grain size and tempering effects on the dislocation density of low-C Nb–Ti microalloyed lath martensite. *Scr. Mater.* **2015**, *107*, 123–126. [CrossRef]
21. Li, S.; Xi, X.; Luo, Y.; Mao, M.; Shi, X.; Guo, J.; Guo, H. Carbide precipitation during tempering and its effect on the wear loss of a high-carbon 8 Mass% Cr tool steel. *Materials* **2018**, *11*, 2491. [CrossRef] [PubMed]
22. Bhadeshia, H.; Honeycombe, R. *Steels: Microstructure and Properties*; Butterworth-Heinemann: Cambridge, MA, USA, 2017.
23. Candelaria, A.F.; Pinedo, C.E. Influence of the heat treatment on the corrosion resistance of the martensitic stainless steel type AISI 420. *J. Mater. Sci. Lett.* **2003**, *22*, 1151–1153. [CrossRef]
24. Hunkel, M.; Dong, J.; Epp, J.; Kaiser, D.; Dietrich, S.; Schulze, V.; Rajaei, A.; Hallstedt, B.; Broeckmann, C. Comparative study of the tempering behavior of different martensitic steels by means of in-situ diffractometry and dilatometry. *Materials* **2020**, *13*, 5058. [CrossRef] [PubMed]
25. Nolze, G.; Winkelmann, A.; Cios, G.; Tokarski, T. Tetragonality mapping of martensite in a high carbon steel by EBSD. *Mater. Charact.* **2021**, *175*, 111040. [CrossRef]
26. Jumov, G.V. Martensite crystal lattice, mechanism of austenite-martensite transformation and behavior of carbon atoms in martensite. *Metall. Trans. A* **1976**, *7*, 999–1011. [CrossRef]
27. Cheng, L.; Böttger, A.; De Keijser, T.H.; Mittemeijer, E.J. Lattice parameters of iron-carbon and iron-nitrogen martensites and austenites. *Scr. Metall. Mater.* **1990**, *24*, 509–514. [CrossRef]
28. Maruyama, N.; Tabata, S.; Kawata, H. Excess solute carbon and tetragonality in as-quenched Fe-1Mn-C (C: 0.07 to 0.8 mass pct) martensite. *Metall. Mater. Trans. A* **2020**, *51*, 1085–1097. [CrossRef]
29. Christian, J.W. Tetragonal martensites in ferrous alloys—A critique. *Mater. Trans. JIM* **1992**, *33*, 208–214. [CrossRef]
30. Han, K.; Van Genderen, M.J.; Böttger, A.; Zandbergen, H.W.; Mittemeijer, E.J. Initial stages of Fe-C martensite decomposition. *Philos. Mag. A* **2001**, *81*, 741–757. [CrossRef]
31. Mishra, A.; Maity, J. Structure–property correlation of AISI 1080 steel subjected to cyclic quenching treatment. *Mater. Sci. Eng. A* **2015**, *646*, 169–181. [CrossRef]

32. Meysami, A.H.; Ghasemzadeh, R.; Seyedein, S.H.; Aboutalebi, M.R. An investigation on the microstructure and mechanical properties of direct-quenched and tempered AISI 4140 steel. *Mater. Des.* **2010**, *31*, 1570–1575. [CrossRef]
33. Huber, F.; Bischof, C.; Hentschel, O.; Heberle, J.; Zettl, J.; Nagulin, K.Y.; Schmidt, M. Laser beam melting and heat-treatment of 1.2343 (AISI H11) tool steel–microstructure and mechanical properties. *Mater. Sci. Eng. A* **2019**, *742*, 109–115. [CrossRef]